Medical Image Analysis 39 (2017) 44–55

Contents lists available at ScienceDirect

Medical Image Analysis

journal homepage: www.elsevier.com/locate/media

Fully-automatic left ventricular segmentation from long-axis cardiac cine MR scans

Rahil Shahzad[a,1,*], Qian Tao[a,1], Oleh Dzyubachyk[a], Marius Staring[a], Boudewijn P.F. Lelieveldt[a,b], Rob J. van der Geest[a,2]

[a] Division of Image Processing, Department of Radiology, Leiden University Medical Center, PO Box 9600, 2300 RC, Leiden, The Netherlands
[b] Intelligent Systems Department, Delft University of Technology, PO Box 5031, 2600 GA, Delft, The Netherlands

ARTICLE INFO

Article history:
Received 23 January 2017
Revised 10 April 2017
Accepted 12 April 2017
Available online 13 April 2017

Keywords:
Atlas-based segmentation
Registration
Cardiac MRI
Left ventricular segmentation
Long-axis cine MRI

ABSTRACT

With an increasing number of large-scale population-based cardiac magnetic resonance (CMR) imaging studies being conducted nowadays, there comes the mammoth task of image annotation and image analysis. Such population-based studies would greatly benefit from automated pipelines, with an efficient CMR image analysis workflow. The purpose of this work is to investigate the feasibility of using a fully-automatic pipeline to segment the left ventricular endocardium and epicardium simultaneously on two orthogonal (vertical and horizontal) long-axis cardiac cine MRI scans. The pipeline is based on a multi-atlas-based segmentation approach and a spatio-temporal registration approach. The performance of the method was assessed by: (*i*) comparing the automatic segmentations to those obtained manually at both the end-diastolic and end-systolic phase, (*ii*) comparing the automatically obtained clinical parameters, including end-diastolic volume, end-systolic volume, stroke volume and ejection fraction, with those defined manually and (*iii*) by the accuracy of classifying subjects to the appropriate risk category based on the estimated ejection fraction. Automatic segmentation of the left ventricular endocardium was achieved with a Dice similarity coefficient (DSC) of 0.93 on the end-diastolic phase for both the vertical and horizontal long-axis scan; on the end-systolic phase the DSC was 0.88 and 0.85, respectively. For the epicardium, a DSC of 0.94 and 0.95 was obtained on the end-diastolic vertical and horizontal long-axis scans; on the end-systolic phase the DSC was 0.90 and 0.88, respectively. With respect to the clinical volumetric parameters, Pearson correlation coefficient (R) of 0.97 was obtained for the end-diastolic volume, 0.95 for end-systolic volume, 0.87 for stroke volume and 0.84 for ejection fraction. Risk category classification based on ejection fraction showed that 80% of the subjects were assigned to the correct risk category and only one subject ($<$ 1%) was more than one risk category off. We conclude that the proposed automatic pipeline presents a viable and cost-effective alternative for manual annotation.

1. Introduction

1.1. Background

Cardiovascular related complications are quite common throughout the world (Mendis et al., 2011; Celermajer et al., 2012). For better understanding of cardiovascular diseases and screening, large population-based cohort studies are gaining popularity (Fox et al., 2009; Hegenscheid et al., 2009; Jefferson et al., 2011; Bamberg et al., 2015). Cardiac magnetic resonance (CMR) does not have harmful ionizing radiation, does not require contrast materials and can be used to obtain a number of anatomical and functional parameters. This is the most preferred imaging modality among population-based studies.

Common CMR protocols include three cine scans: a horizontal long-axis cine (HLA), also called a four-chamber view, a vertical long-axis cine (VLA), also called a two-chamber view, and a short-axis (SAX) stacked cine (Alfakih et al., 2004). The HLA and VLA scans are acquired in 2D over a number of cardiac phases, and can be represented as 2D+t image series. The SAX scan is acquired in the form of multiple 2D+t stacks that cover the entire heart region from the base to the apex. A SAX scan can be reconstructed as a 3D+t scan.

* Corresponding author.
E-mail address: r.shahzad@lumc.nl (R. Shahzad).
[1] Both authors contributed equally to this work.
[2] Submitted on behalf of the Heart Brain Connection Collaborative Research Group.

http://dx.doi.org/10.1016/j.media.2017.04.004
1361-8415/

With hundreds and thousands of subjects being included in large population studies (Bild et al., 2002; Victor et al., 2004; Taylor Jr et al., 2005; Petersen et al., 2016) and, with multiple CMR scans for each subject, it would be very desirable to have automatic pipelines that can accurately segment and quantify the cardiac structures from these scans.

A number of (semi-)automated methods that segment various structures from the SAX scan are proposed in the literature (Petitjean and Dacher, 2011). As the SAX cine scan covers the entire heart region in 3D, this enables accurate segmentation of the cardiac structures in 3D+t.

Breath-holds are required for the duration of each 2D+t acquisition to reduce breathing artifacts (Sakuma et al., 1993). As SAX scans require multiple 2D+t images, the acquisition of SAX scans is time consuming. A typical acquisition time for the short-axis scan is about 5 min, including the breathing instructions. For the long-axis scan the acquisition time is about 20 s for each view. Also, the breath-hold approach is not ideal for subjects who cannot hold their breath for long periods of time. Processing of these scans is also difficult and time consuming due to the inability of accurately identifying the base and apex of the heart through the cardiac cycle. Koikkalainen et al. (2004) demonstrated that combining SAX scans with multi-slice long-axis scans (LAX) resulted in a higher segmentation accuracy of the chambers. However this method was validated on static 3D volumetric SAX and LAX scans, which require longer acquisition times. Childs et al. (2011) have shown that left ventricular (LV) parameters were more reproducible and time saving when multiple (up to 6 radial) long-axis acquisitions were used. Using long-axis views makes it much easier to detect the extremities of the LV. It has also been shown in literature that 2D+t long-axis HLA and VLA scans can be used to obtain fast and accurate measurements of LV function (Bloomer et al., 2001). Another study by Huttin et al. (2015) have demonstrated that the LV volumetric measures obtained from the two orthogonal 2D+t HLA and VLA scans have very good correlation when compared to the 3D+t SAX scan. These methods were based on manual annotation, however.

1.2. Proposed work

In this paper, we present a fully-automatic method that can segment the LV endocardium and epicardium from the 2D+t HLA and VLA cine scans simultaneously. Cardiac volumetric parameters are derived by combining the segmentations from both cine scans. This automatic method can facilitate fast and accurate analysis of the cardiac function. To the best of our knowledge, no methods that segment the LV in a fully-automatic manner on long-axis 2D+t HLA and VLA cine scans have been developed until now.

The proposed method is broadly based on a multi-atlas-based segmentation approach and a spatio-temporal registration approach, with refinements based on mathematical programming. The pipeline was trained on 10 subjects, which were also used as atlas scans. The method was further evaluated on 145 subjects with respect to: (*i*) accuracy of the contour detection on both the end-diastolic phase and the end-systolic phase, (*ii*) quantification accuracy of the clinically relevant parameters, (*iii*) performance of the method with respect to the inter-observer variability on the volumetric clinical parameters, and (*iv*) comparing the clinical parameters derived from the HLA and VLA scans to those obtained using the SAX scans.

2. Materials and methods

Our method is broadly divided into five stages: (*i*) an image preprocessing step; to correct for the tissue intensity differences across the scans (Section 2.3), (*ii*) an atlas-based segmentation step; for obtaining the LV endocardium and epicardium contours on the end-diastolic phase (Section 2.4), (*iii*) a contour refinement step; for fine-tuning the obtained atlas-based contours (Section 2.5), (*iv*) a contour propagation step; a group-wise registration approach to propagate the contours from the end-diastolic phase to each of the remaining phases, amongst others to identify the end-systolic phase (Section 2.6) and (*v*) a valve detection step; to distinguish between the left ventricle and the left atrium in the end-systolic phase, for accurate LV endocardium measurements (Section 2.7). Fig. 1 provides a flowchart of the proposed workflow. Before the above methodological steps are explained in detail, we begin with describing our study data and reference standard in Sections 2.1 and 2.2.

2.1. Data

The data used in our study comes from the multi-center heart-brain connection cohort (The heart-brain connection) (van Buchem et al., 2014). Four medical centers situated in The Netherlands: VU Medical Center (VUMC), Leiden University Medical Center (LUMC), Maastricht University Medical Center (MUMC) and University Medical Center Utrecht (UMCU) were involved in scanning the subjects. Each of the centers used a 3T MRI scanner from the same vendor, Philips Medical System (Best, The Netherlands). However, the scanner models were different: LUMC used an Ingenia 3.0T, MUMC and UMCU both used an Achieva 3.0T and VUMC used an Ingenuity TF scanner. Each center was instructed to follow the same protocol to scan the subjects. Various scans for both the brain and the heart were acquired at each of the centers. For details about the scans acquired and the selection criteria for the subjects the readers are referred to the publication of van Buchem et al. (2014).

For this work, a total of 145 subjects were included, and only the HLA and VLA scans were used for building and evaluating the proposed framework. These scans were acquired using the sensitivity encoding protocol (SENSE) (Pruessmann et al., 1999) with a balanced ultra-fast gradient echo imaging mode (sB-TFE). ECG gating and breath-holding were also used. The 2D+t cine scans were acquired with 40 time points (phases) each, a pixel size of 1.75×1.75 mm^2 and a slice thickness of 8 mm. The flip angle was 45°, TR/TE=3.6/1.81 ms and FOV=400 × 400 mm. Average acquisition time for each long-axis cine scan was 9 s.

Characteristics of the included subjects are presented in Table 1. Note, that only 13 subjects were healthy controls, whereas the remaining subjects had various clinical anomalies. Total number of subjects with heart failure was 53, 33 of these subjects were ischemic and 20 were non-ischemic. Furthermore, 14 subjects had coronary angioplasty (PTCA) and 11 had a bypass (CABG) intervention.

Table 1
Population characteristics. The included subjects fall in four categories: healthy controls, subjects with carotid occlusive disease (COD), subjects with vascular related cognitive impairment (VCI) and subjects with heart failure.

Variable	Value
Sample size	145
Men	91 (62.8%)
Age, range	67.5 (50–90)
Controls	13 (8.9%)
COD	27 (18.6%)
VCI	52 (35.9%)
Heart Failure	53 (36.6%)
Ischemic	33
Non-ischemic	20
PTCA	14
CABG	11

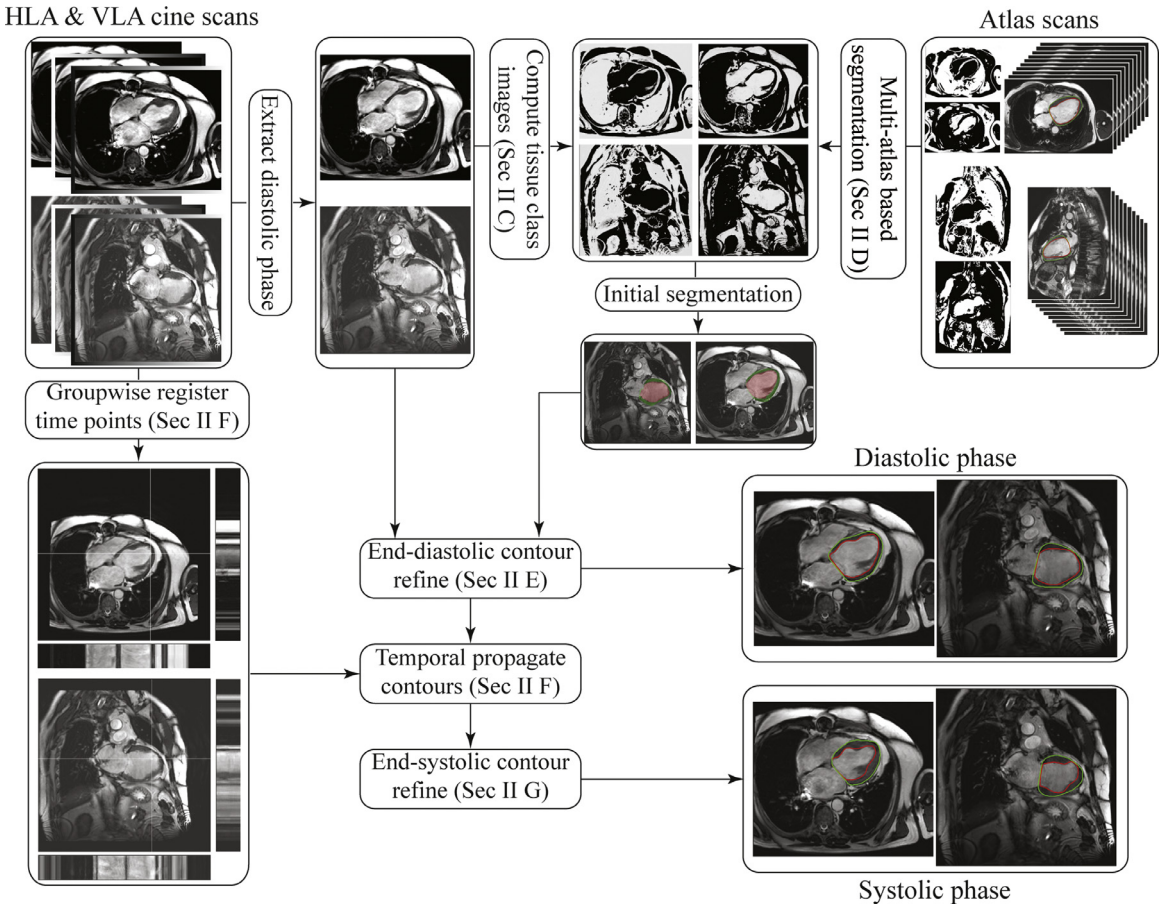

Fig. 1. The schematic shows the entire workflow of our proposed pipeline; starting from atlas-based segmentation, contour refinement and propagation, to volumetric quantification.

2.2. Reference standard

For all the data sets used in our study, two experienced observers manually delineated the endocardial and epicardial contours on the end-diastolic and end-systolic phases of the HLA and VLA cine scans using consensus decision. Important clinically relevant parameters are derived from the end-diastolic and end-systolic phases, hence only these two phases were manually annotated. An in-house developed software tool MASS (LUMC) was used for the manual annotation.

2.3. Image preprocessing

A preprocessing step was performed on the *end-diastolic* phase of both the HLA and the VLA scan, to improve the accuracy of the multi-atlas-based segmentation described in Section 2.4. The reason for this preprocessing step is to correct for the tissue intensity differences across the scan caused by the intensity inhomogeneity (scanner bias). Typical segmentation methods require a region of interest (ROI) to be defined for the chamber that the algorithm is being targeted. Our approach does not require such a ROI, the entire field of view (FOV) of the HLA and VLA scan is being used.

Each of the HLA and VLA volumes was initially smoothed by a 3×3 median filter. Then we ran 50 iterations of the Coherent Local Intensity Clustering (CLIC) method (Li et al., 2009), which is essentially a fuzzy-c-means clustering method with built-in intensity inhomogeneity correction. The CLIC algorithm was initialized by providing initial values for the centers of the background and foreground clusters. The latter were estimated by applying Otsu threshold (Otsu, 1975) to the image cropped to the largest rectangle that excludes potentially non-sampled regions. Other parameter values of the CLIC method were: number of classes c=2, standard deviation of the Gaussian kernel σ=10, fuzzyfier q=2. Class membership functions calculated by the CLIC algorithm (see Fig. 2) were used as probability maps in further processing steps.

2.4. Atlas-based segmentation

An atlas-based segmentation (Aljabar et al., 2009) approach was used to segment the LV endocardium and epicardium at the *end-diastolic* phase of the HLA and VLA scans. The first image in the 2D+t cine scan was assumed to represent the moment of end-diastole. HLA and VLA scans from ten additional subjects were used to generate a set of atlases. The atlases were chosen across the population based on the quality of the scan, health condition of the heart and, the anatomical variation that was representative for the general population. For each atlas, observers manually delineated the endocardial and epicardial contours on both views at the *end-diastolic* phase. An overview of the atlases and the manual contours is shown in Fig. 3.

Each of the ten atlases was registered (Suri et al., 2007; Rohlfing et al., 2005) to the unseen subjects' corresponding end-diastolic HLA and VLA scans. In the registration procedure, the transformation parameters $\hat{\mathbf{T}}$ that minimize the dissimilarity $\mathcal{C}(\mathbf{T}; F, M)$ between the fixed image (F) and the moving image (M) are determined. The optimization problem can be mathematically represented as:

$$\hat{\mathbf{T}} = \arg\min_{\mathbf{T}} \mathcal{C}(\mathbf{T}; F, M). \quad (1)$$

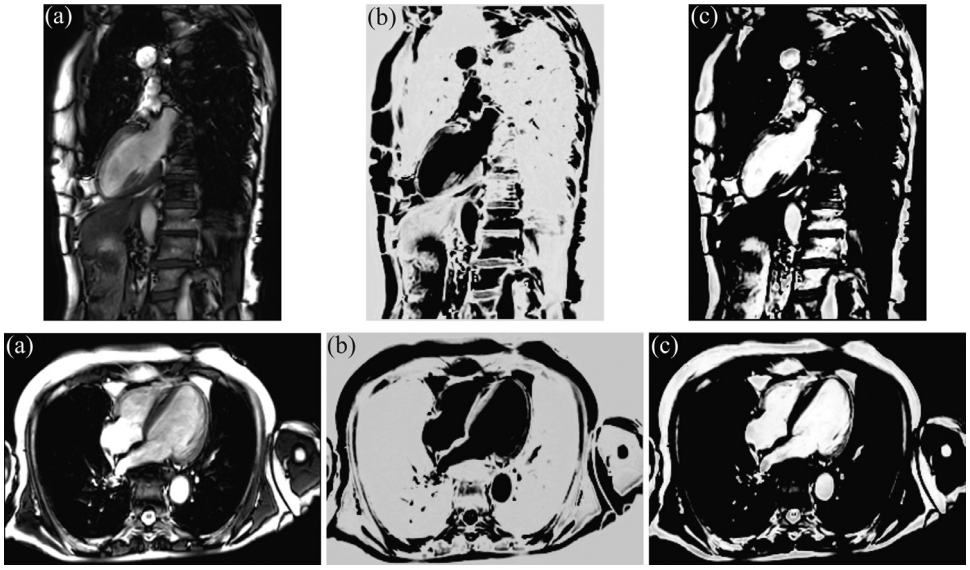

Fig. 2. Overview of the preprocessing steps. The original VLA and HLA scans (a). The two probability images: tissue class (b) and blood-and-fat class (c); black color represents low probability values.

Once all the atlases are registered to the subject, the resulting transformation $\hat{\mathbf{T}}$ from the registration is used to map the endocardium and epicardium contours from each of the atlas scans (A) onto the subject scan (S).

In our pipeline, the calculated probability tissue class images of both the subject and the atlases were used for registration. Atlas scans were used as fixed images and subjects' scans were used as moving images.

A two-stage registration approach was used. In the first stage, an affine transformation was used to approximately align the subject scan and the atlas scans. In the second stage, a non-rigid registration using a B-spline transformation was employed while using the results of the affine transformation to initialize the registration. A multi-resolution approach, in a coarse-to-fine manner using up to three resolutions was used. Adaptive stochastic gradient descent (Klein et al., 2009) was used for optimization. The number of voxels sampled in each iteration was set to 2048, and the number of iterations was set to 512 for the affine transformation and 2048 for the B-spline transformation. A fixed mask in the form of a rectangular box that covers the entire heart on the atlas scans was used as the fixed mask during registration. All registrations were performed using the publicly available registration software `elastix` (Klein et al., 2010).

The final endocardium and epicardium contours were obtained by combining the transformed labels by using a label fusion strategy. A number of label fusion strategies exist in literature, the most common ones being majority vote (Lam and Suen, 1997) and simultaneous truth and performance level estimation (STAPLE) (Warfield et al., 2002; Rohlfing et al., 2004). In this work, we used a variation of STAPLE described by Klein et al. (2008).

2.5. End-diastolic contour refinement

Multi-atlas-based segmentation yields accurate segmentation of the LV, especially in terms of the endocardial border. The epicardial border, however, is relatively coarse and requires further refinement. In this study, we introduce a contour refinement process to correct the *end-diastolic epicardial* contour based on local intensities of individual MR scans and using an energy minimization framework.

Firstly, the local image intensity in the proximity of the epicardial contour is extracted by sampling the image intensity along the profile lines perpendicular to the initial endocardial contour, as illustrated in Fig. 4c. In this study, 500 profile lines evenly-distributed along the endocardial contour were computed. Smoothing of the endocardial contour was applied to ensure smooth transition of the sampling line directions. From the original image (Fig. 4a) it can be seen that the epicardial border is defined by edges resulting from soft tissue contrast, both bright-to-dark and dark-to-bright, as well as dark lines caused by chemical shift (Hood et al., 1999). The former are marked by red arrows and the latter by yellow arrows. For better visualization, a profile view with the corresponding arrows is shown in Fig. 4d.

Secondly, the image energy for capturing the epicardial border was defined:

$$E = E_{ed} + E_{cs} + \alpha E_{sm}, \tag{2}$$

where E_{ed} denotes energy of the soft tissue edge, E_{cs} denotes energy of dark lines from chemical shift and E_{sm} denotes smoothness of the contour that will be enforced during the optimization with a weighting term α. To compute E_{ed}, a first-order Gaussian derivative filter bank is applied to the profile image. To compute E_{cs}, a second-order Gaussian derivative filter bank is applied to the profile image. The filter bank consists of a set of directional filters, with a range of directions that are considered to be likely for the epicardial contour, to suppress noisy edges in random directions. The filter bank works as follows:

$$E_{ed}(P) = -\max_{\theta\in\Theta}\{|P * F_{G1}(\theta)|\}, \tag{3}$$

$$E_{cs}(P) = -\max_{\theta\in\Theta}\{P * F_{G2}(\theta)\}, \tag{4}$$

where P is the profile image, $F_{G1}(\theta)$ is the first-order Gaussian filter bank that is sensitive to edges, and $F_{G2}(\theta)$ is the second-order Gaussian filter bank that is sensitive to dark lines. In both functions, θ takes values in a range Θ. In this work, Θ was set to be within $[-15^\circ, 15^\circ]$ with the increment of 1° as the epicardial contour is expected to be roughly parallel to the endocardial contour. The maximal response of these filters was taken as the energy output. Note that for E_{ed} the absolute value of the response is taken since the edge can be either bright-to-dark or dark-to-bright. Fig. 5a and b show the computed energy function E_{ed} and E_{cs} from the profile image.

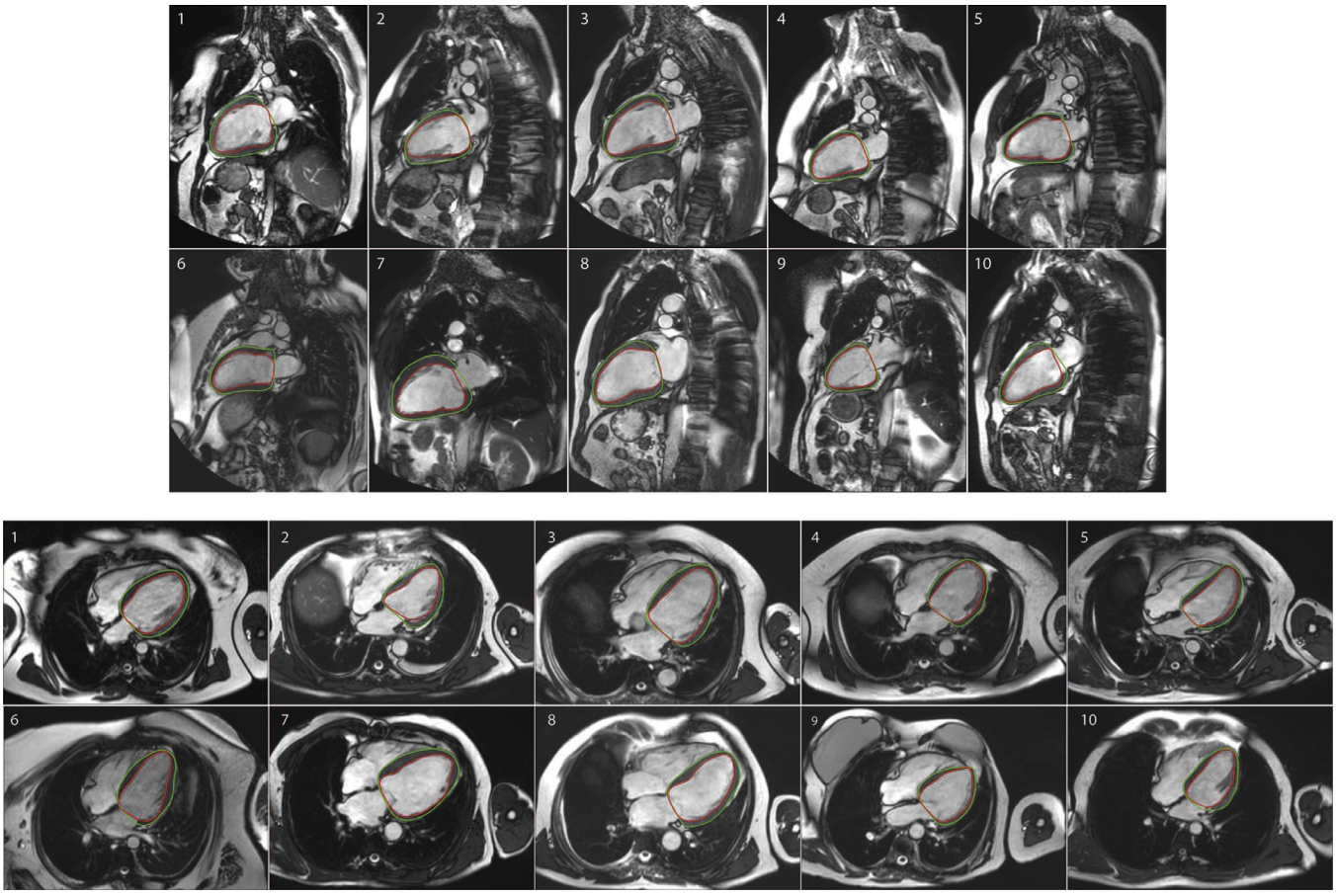

Fig. 3. Different atlas scans used for the multi-atlas-based segmentation method. The numbers indicate the corresponding VLA (top) and HLA (bottom) scans of the same atlas. The red and the green lines are the manually drawn endocardial and epicardial contours, respectively. (For interpretation of the references to color in this figure legend, the reader is referred to the web version of this article.)

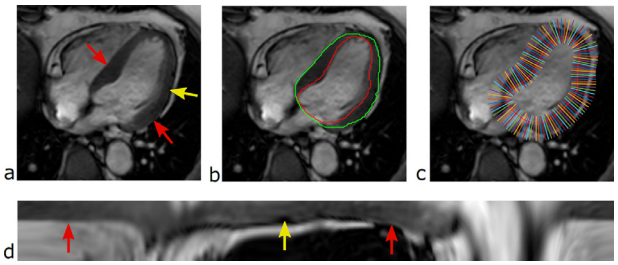

Fig. 4. A random diastolic HLA MR image (a). The initial endocardial and epicardial contours obtained after the multi-atlas segmentation (b). The sampling profile lines computed from the smoothed endocardial contour (c). The profile image resulting from sampling along the profile lines (d). Red arrows indicate edges of soft tissue, while yellow arrows indicate dark lines caused by chemical shift. (For interpretation of the references to color in this figure legend, the reader is referred to the web version of this article.)

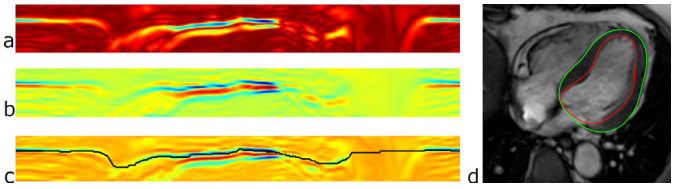

Fig. 5. The energy E_{ed} computed from the profile image (a). The energy E_{cs} computed from the profile image (b). Low values in E_{ed} and E_{cs} indicate likely locations of epicardial contour. The Dijkstra's search result on $E_{ed} + E_{cs}$ (c). The search result projected back onto the original image as the refined epicardial contour (d).

Finally, Dijkstra's algorithm (Dijkstra, 1959) was adopted to search for the optimal track through the matrix $E_{ed} + E_{cs}$, which minimizes the sum of energy along its way. During the search, the term E_{sm} is computed as the length of the contour in polar coordinates to penalize abrupt changes and shaky lines. The term E_{sm} is also weighted using α which takes an empirical value of $2 \times B$, where B is the average signal intensity of the blood pool. This weighting term ensures that E_{sm} is comparable to E_{ed} and E_{cs} by adapting to the signal intensity range of each individual MR data set. This method is able to find the globally-optimal solution with low computational complexity. Fig. 5c shows the results of the search, while Fig. 5d shows the corresponding epicardial contour on top of the original HLA image. Note that the contour refinement step is applied on both views separately and on the end-diastolic phase only.

2.6. Contour propagation through the cardiac cycle

Once the refined endocardium and epicardium contours on the *end-diastolic* phase are obtained, the next step was to propagate the contours throughout the cardiac cycle. For this, image registration was used once again. In the current scenario, the different phases (or time points) of a scan are registered to each other in a group-wise manner. The obtained deformations can subsequently be used to propagate the refined contours from the end-diastolic phase to all other phases.

A number of methods that present different ways of registering dynamic image sequences are already available in literature. Two recent review papers by McClelland et al. (2013) and

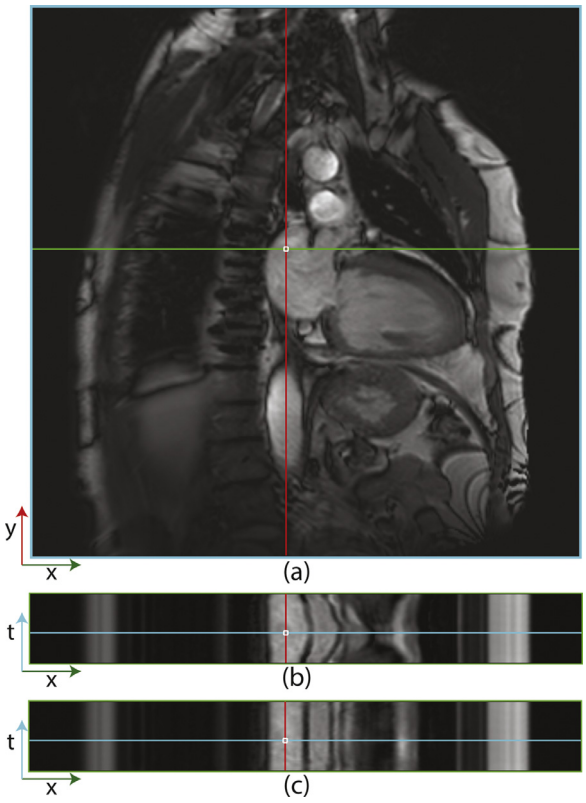

Fig. 6. A VLA scan of a subject (a), the cross-hair on the figure indicates a location with substantial motion. The reformatted image stacked over the different phases before (b) and after registration (c).

Sotiras et al. (2013) summarize these methods. One of the most promising approaches is the one proposed by Metz et al. (2011). This method incorporates both spatial and temporal dimensions with the aim to minimize the change of image intensity over time. The proposed method uses a Lagrangian nD+t B-spline transformation model. The method searches for the B-spline transformation that aligns all the cardiac phases to a reference phase by minimizing the variance of voxel intensity values over time.

Three steps are required to propagate the contours from the end-diastolic phase to the rest of the cardiac cycle. Firstly, all cardiac phases are registered to each other (forward transformation) in a group-wise manner (Metz et al., 2011). Secondly, the inverse transformation is computed in order to determine the coordinate mapping from each of the cardiac phases to the end-diastolic phase. Finally, both the forward and the inverse transformations are combined such that contour points from the end-diastolic phase can be transformed to all the other phases. For further details readers are referred to the work of Metz et al. (2011).

Fig. 6 shows an example subject before and after applying the group-wise registration (forward transformation). Fig. 6b shows the unregistered reformatted image along the horizontal axis, stacked over the entire cardiac cycle (40 phases), where the vertical lines are deformed due to the motion of the beating heart. It can be appreciated from Fig. 6c that our registration model captures the heart motion very accurately.

2.7. End-systolic contour refinement

The contour propagation step works well. The registration method is able to capture the cardiac motion and helps in propagating the endocardial and epicardial contours throughout the cardiac cycle. The *end-systolic* phase can then be determined from the cine scans using the size of the propagated contours.

Since no prior information about the left atrium (LA) is provided to the spatio-temporal registration method, it cannot accurately differentiate between the LV and LA. Hence, when the contours are propagated, they slightly overestimate the LV size on the end-systolic phase. Thus, a mitral valve detection algorithm is introduced to correct for this overestimation.

The valve detection algorithm has the following steps. Initially, the end-systolic phase is automatically determined by selecting the phase that has the smallest endocardial (propagated) contour area (see Fig. 7). Using this contour, the major axis of the endocardium is determined and an intensity profile along this axis is calculated. Next, exploiting the fact that the mitral valve is always closed at the end-systolic phase, it is safe to assume that there will be a sudden drop in the intensity profile at the blood-valve interface. By using a regression curve fitting along the intensity profile, the location of the blood-valve interface can be detected (as shown in Fig. 7b). A regression fit along the intensity profile is required to smooth out the noisy raw data. Last, a perpendicular line through the major axis at the detected intensity drop would give us the location of the mitral valve. This information is used to correct the LV endocardial contour on the end-systolic phase. Fig. 7 shows a random subject with the systolic VLA scan, along with the endocardial contour after the contour propagation stage, the intensity profile and the detected mitral valve location.

2.8. Quantification of volumetric parameters

Once our entire pipeline has run on both the VLA and HLA cine scans, a number of clinical parameters were calculated from the processed data. Volumetric parameters can be obtained from the two orthogonal VLA and HLA scans by using the well known biplane area-length method (Dulce et al., 1993; Pujadas et al., 2004). More precisely, for each of the cine scans, the area and the length (major axis) of the endocardium are calculated. Volumetric information can be derived using the following equation:

$$V = \frac{8A_2A_4}{3\pi L_{min}}, \tag{5}$$

where A_2 and A_4 is the corresponding VLA and HLA scans' segmented area and L_{min} is the smallest major axis length of the VLA and HLA scans' segmented region.

By applying Eq. (5), on the end-diastolic and end-systolic phases for the endocardial contour the corresponding end-diastolic volume (EDV) and end-systolic volume (ESV) can be derived.

Stroke volume (SV) is calculated as:

$$\mathrm{SV} = \mathrm{EDV} - \mathrm{ESV}.$$

Ejection fraction (EF) is obtained by:

$$\mathrm{EF} = \frac{\mathrm{SV}}{\mathrm{EDV}} \times 100.$$

Based on the left ventricular EF value, the subject can be assigned to one of the clinically relevant categories: normal (EF $\geq$ 50%), mild dysfunction (EF = 40% to 49%), moderate dysfunction (EF = 30% to 39%) and severe dysfunction (EF $<$ 30%).

3. Experiments and results

3.1. Experiments on atlas scans

A number of experiments were performed during the building and evaluation stages of the pipeline. In this section we present the experiments that were conducted. For these experiments, only the ten *atlas scans* were used to optimise and validate the pipeline.

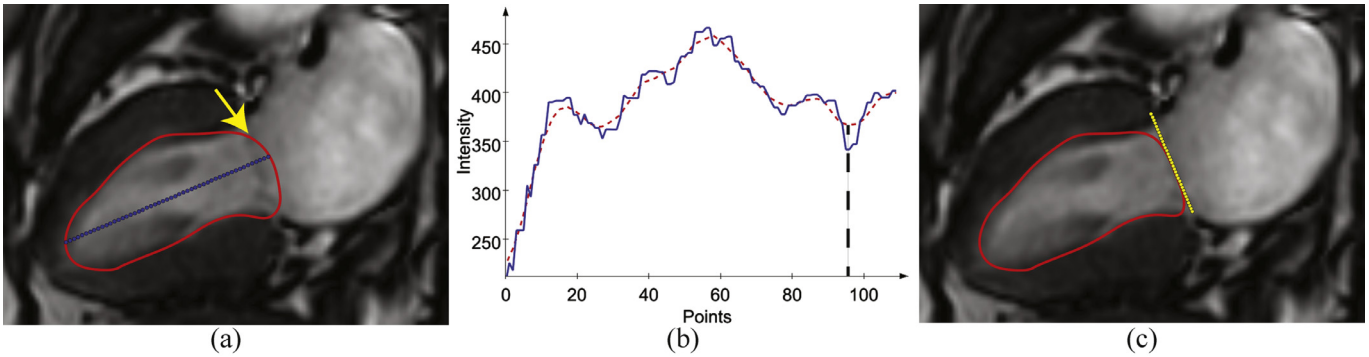

Fig. 7. A VLA scan along with the propagated end-systolic endocardium contour (in red) and the major axis (in blue), with an arrow pointing at the location of the closed mitral valve (a). The intensity profile along the major axis (in blue), a regression fit (in red) and detected valve intersection (in black) (b). The same VLA scan after contour refinement with the identified mitral valve location overlayed (in yellow) (c). (For interpretation of the references to color in this figure legend, the reader is referred to the web version of this article.)

Table 2
Leave-one-out experiment on the atlas set to compare the registration strategies (*Original scan* and *Probability image* represent the two registration scenarios) and the improvement after applying the epicardial contour refinement on the probability image result (Section 2.5) in terms of the Dice similarity coefficient (DSC), maximum surface distance (MaxD) and mean surface distance (MSD). Distances are reported in mm.

View	DSC	MaxD	MSD
VLA ED endocardium			
Original scan	0.85	10.4	2.8 ± 2.6
Probability image	0.95	4.8	1.6 ± 1.1
Contour refine	0.95	4.3	1.0 ± 1.1
VLA ED epicardium			
Original scan	0.85	10.5	3.2 ± 2.7
Probability image	0.93	6.7	2.2 ± 1.5
Contour refine	0.96	5.4	1.2 ± 1.3
HLA ED endocardium			
Original scan	0.95	5.4	1.4 ± 1.3
Probability image	0.96	4.2	1.5 ± 0.9
Contour refine	0.96	3.2	0.9 ± 0.8
HLA ED epicardium			
Original scan	0.93	6.9	1.6 ± 1.6
Probability image	0.96	4.7	1.6 ± 1.1
Contour refine	0.96	3.8	0.9 ± 0.9

In Sections 2.3 and 2.4 we proposed that using the probability tissue class images would improve the accuracy of the multi-atlas-based segmentation, in the experiments we also report the quantitative proof for such a choice by running our method on the original MR images. Leave-one-out experiments were conducted on the VLA and HLA atlas scans. For both cases, i.e. the one using the original MRI scans and the one using the probability tissue class images, a two-stage registration approach was used, as explained in Section 2.4. For the original MRI scans, mutual information was used as similarity measure for the cost function, whereas normalized correlation was used for the probability images. For both scenarios, a fixed mask was used. Preliminary results showed that registration results were much better when a mask was used.

From the above experiment, it was observed that the segmentation accuracy was much better when the preprocessed tissue probability images are used for multi-atlas-based segmentation. Table 2 shows the DSC and the surface distance errors by comparing the automatically obtained contours with those obtained manually. As the atlas scans were created on the end-diastolic phase, the numbers from the table correspond to this phase.

The next experiment was to quantify the improvement of the end-diastolic contours. For this, the contour refinement step (Section 2.5) was applied to the contours obtained using the tissue probability images. From Table 2 we can observe that applying the contour refinement step further improves the segmentation accuracy.

All experiments presented in Table 2 were performed on the end-diastolic images only. Thus, a final experiment was performed to validate the contour propagation step. Experiments were performed with and without the end-systolic mitral valve detection step (Section 2.7). The DSC was computed on the atlas scans between the manually drawn contours and the ones obtained automatically. Fig. 8 shows the DSC for the endocardial and epicardial contours, after the contour propagation step. The average DSC on both views and both contours was around 0.95 on the end-diastolic phase (D Endo, D Epi) and 0.89 on the end-systolic phase (S Endo, S Epi) before mitral valve detection. The DSC on the end-systolic phase after the mitral valve detection step was 0.92.

From the above experiments, the benefit of using each of the intermediate refinement steps in our pipeline was demonstrated on the atlas set. Further validation on the entire test data set (145 subjects) was thus performed using the multi-atlas-based segmentation on the probability tissue class images and with refinement of the end-diastolic and end-systolic contours.

3.2. Agreement between the automatic method and the ground truth on the test data

A visual check showed that the pipeline was successful on 94% (136) of the data sets. The nine failed cases had imaging artefacts and were excluded from further analysis.

A number of quantitative parameters were derived from both the manually obtained contours and the automatically derived contours.

First, we compare the segmentation accuracy. Table 3 provides the segmentation performance over the entire test data set. The DSC on the end-diastolic (ED) phase is around 0.94 on both views and for both the endocardium and epicardium contours. On the end-systolic (ES) phase the DSC ranges between 0.85 and 0.90. Fig. 9 shows the corresponding boxplot for the test data set.

Second, we compare the ED and ES endocardium surface area on both views. A Pearson correlation coefficient (R) of 0.94 was obtained between the manual segmentation and the automatic one for the ED VLA area. R of 0.93, 0.92 and 0.90 was obtained for ED HLA, ES VLA and ES HLA area, respectively. Bland-Altman analysis showed that the bias between the two measures is almost zero and the average absolute area difference is around 2.8 cm^2. The average

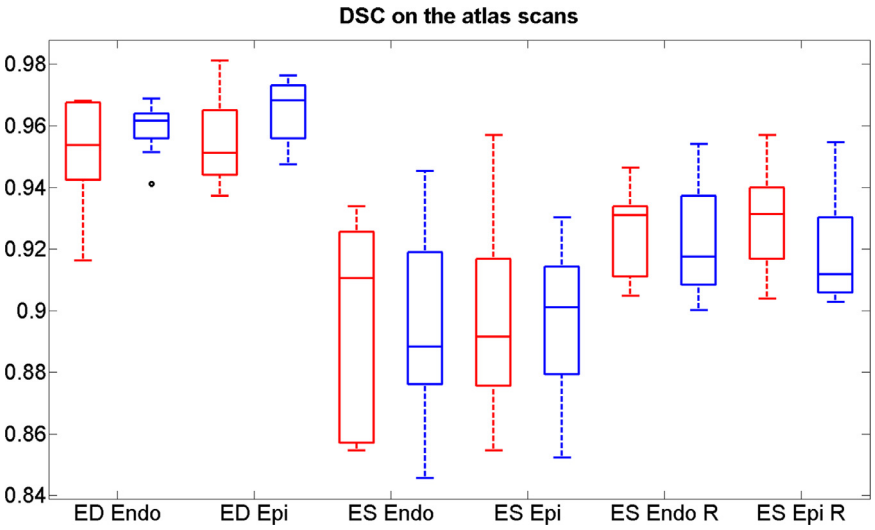

Fig. 8. DSC using leave-one-out analysis over the atlas scans for both the end-diastolic (ED) and end-systolic (ES) phases for the endocardium (Endo) and epicardium (Epi), also after contour refinement (R). The VLA scans are represented in red and the HLA scans in blue. Outlier is represented as a black circle. (For interpretation of the references to color in this figure legend, the reader is referred to the web version of this article.)

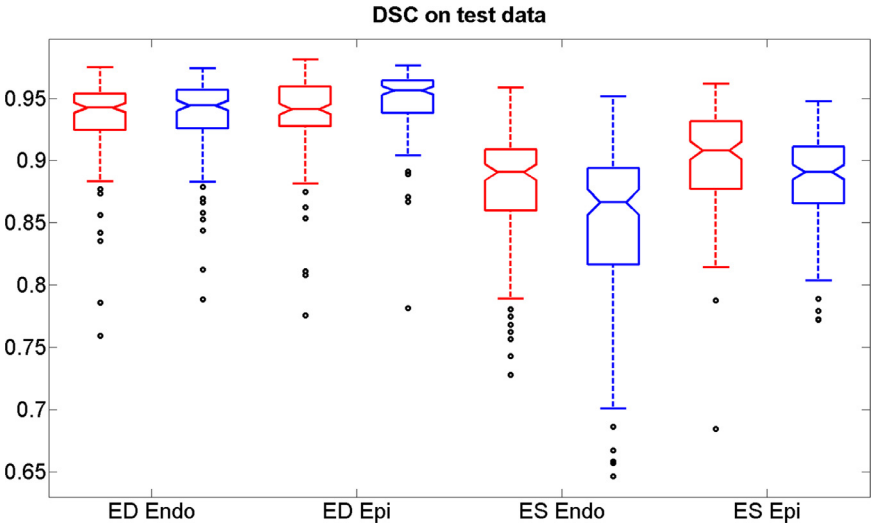

Fig. 9. DSC over all the test data sets. The VLA scans are represented in red and the HLA scans in blue, outliers are represented as black circles. (For interpretation of the references to color in this figure legend, the reader is referred to the web version of this article.)

Table 3
Quantitative segmentation results on the entire data set. Values for endocardium and epicardium contours on both the end-diastolic (ED) and end-systolic (ES) phases are presented in terms of the Dice similarity coefficient (DSC), maximum surface distance (MaxD) and mean surface distance (MSD). Distances reported in mm.

View	DSC	MaxD	MSD
VLA			
ED endocardium	0.93	8.1	2.3 ± 2.1
ED epicardium	0.94	9.1	2.5 ± 2.5
ES endocardium	0.88	6.4	2.7 ± 1.5
ES epicardium	0.90	8.1	3.1 ± 1.8
HLA			
ED endocardium	0.93	7.2	2.2 ± 1.8
ED epicardium	0.95	7.3	2.1 ± 1.9
ES endocardium	0.85	8.2	3.4 ± 2.1
ES epicardium	0.88	8.8	3.7 ± 2.1

ED endocardium area is about 43 cm^2 and ES endocardium area is about 25 cm^2. Detailed performance and quantitative results are presented in Table 4.

Third, we compare the volumetric parameters, namely: the end-diastolic volume (EDV), end-systolic volume (ESV) and stroke volume (SV). *R* of 0.97, 0.95 and 0.90 was obtained for each of the volumes respectively. Bland-Altman analysis showed that the bias for EDV is absent, for ESV is 1.5 ml, and for SV is −1.5 ml. It was also observed that the absolute volume difference between the manual and automatic measure was 12 ± 10 ml for both EDV and ESV, and 10 ± 9 ml for SV. The average EDV is about 172 ml, ESV is 78 ml and SV is 94 ml. Graphical representation of the data for EDV and ESV is shown in Fig. 10.

Fourth, we compare the left ventricular ejection fraction (LVEF). *R* shows an agreement of 0.84. Bland–Altman analysis shows a bias of −1 and the limits of agreement between −15 and 13. Since LVEF is commonly used to categorize the subjects into various risk groups, we generated a confusion matrix. Table 5 presents the results for the categorization of the subjects based on the LVEF. It was observed that 80% of all the subjects were assigned to the correct category, with a weighted Cohen's kappa (κ) agreement of 0.70 (0.51,0.90). It was also observed that only one subject was

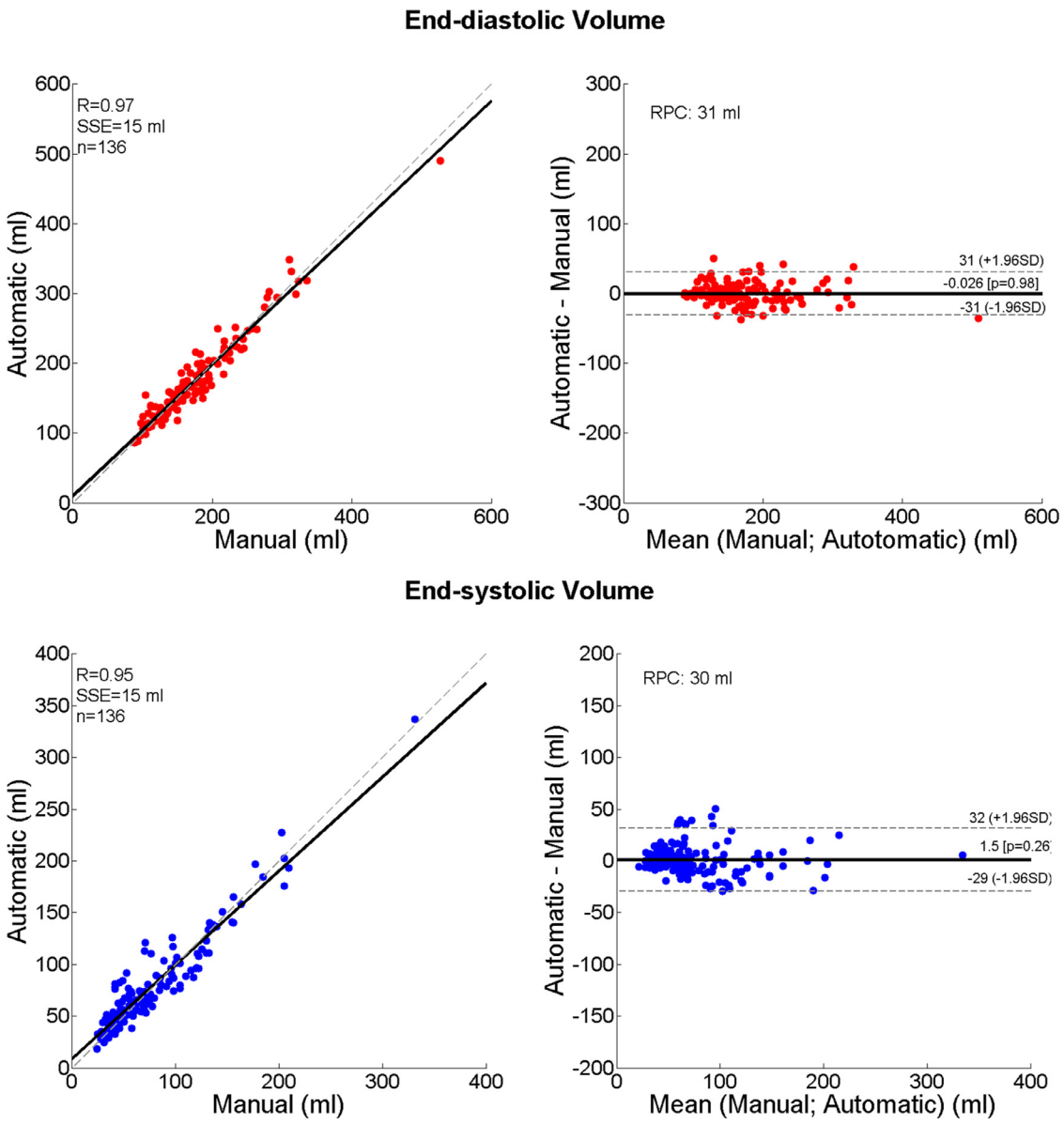

Fig. 10. Scatter plots and Bland–Altman plots for the comparison of the automatic and manual EDV (top) and ESV (bottom). Here, *R* is the Pearson correlation coefficient, SSE is the sum of squared error, *n* is the number of data points and RCP is the reproducibility coefficient.

more than one category off and the majority of the misclassified subjects were borderline cases.

3.3. Interobserver agreement on a subset

To further assess the performance of our automatic framework, interobserver variability was measured on a subset of scans. Thirty-five scans were randomly selected and an independent experienced observer manually annotated the end-diastolic and end-systolic endocardium contours on both views. When the reference standard values were compared to those of the independent observer, calculated *R* was 0.99, 0.98, 0.78 and 0.90 for EDV, ESV, SV and EF, respectively. Absolute difference between the two manually obtained LV volume parameters was: 8.7 ± 10.9, 9.8 ± 8.6, 10.8 ± 16.5 and 8.1 ± 4.1 for EDV, ESV, SV and EF, respectively. Table 6 shows the comparison between the automatic method and the manual contours on a subset, interobserver comparisons are also shown. It can be observed from Table 6 that the calculated statistical parameters are very close to the interobserver variability.

3.4. Agreement between long-axis and SAX volumetric measurements

To gain insights into the differences that emerge from the SAX volumetric quantifications and the bi-plane area-length method of the long-axis quantifications, the volumetric parameters were compared to each other on a subset of 35 scans (same set as used in Section 3.3).

An experienced observer delineated the endocardium on the ED and ES phases of the SAX scan. The observer was instructed to annotate all the slices between the base and the apex of the heart, and to include the papillary muscles as part of the blood pool. Using the manual segmentations four clinical parameters were computed from the SAX scan. These numbers were compared to the corresponding long-axis derived parameters for both, the ground truth values as well as the ones obtained using our proposed pipeline. It was observed that the calculated *R* for the manually

Table 4
Performance of the framework by comparing the automatic method to the reference standard. *R* is the Pearson correlation coefficient along with the linear regression β confidence interval (CI). B-A is the Bland-Altman bias along with the 95% CI, Abs diff is the absolute difference between the automatic method and the manual reference standard. Also the average measures obtained using both the manual (Avg M) and automatic method (Avg A) are reported.

	R (CI for β)	B-A (95% CI)	Avg M	Avg A	Abs diff
ED phase					
VLA area (cm^2)	0.94 (0.92,0.96)	−1 (−7,5)	42.5	41.5	2.4 ± 2.1
HLA area (cm^2)	0.93 (0.90,0.95)	1 (−6,8)	43.4	44.1	2.4 ± 2.5
EDV (ml)	0.97 (0.95,0.98)	0 (−31,31)	172.5	172.4	12 ± 10
ES phase					
VLA area (cm^2)	0.92 (0.88,0.94)	−2 (−9,6)	25.2	23.7	3.2 ± 2.3
HLA area (cm^2)	0.89 (0.84,0.92)	1 (−8,9)	26.3	27.1	3.4 ± 2.9
ESV (ml)	0.95 (0.93,0.96)	2 (−29,32)	78.3	79.8	12 ± 10
SV (ml)	0.87 (0.82,0.91)	−2 (−27,24)	94.1	92.6	10 ± 9
EF (%)	0.84 (0.79,0.89)	−1 (−15,13)	57	56	5.5 ± 4.4

Table 5
Confusion matrix for LVEF category classification between automatic (A) and manual (M) results: normal (I), mild dysfunction (II), moderate dysfunction (III), severe dysfunction (IV).

A\M	I	II	III	IV
I	**88**	6	0	0
II	10	**11**	1	0
III	0	5	**10**	1
IV	0	1	3	**0**

Table 6
Interobserver variability on a subset of 35 subjects. *R* is the Pearson correlation coefficient, SSE is the sum of squared errors, B-A is the Bland-Altman bias, RCP is the reproducibility coefficient, Abs diff is the average absolute difference. Volumes are reported in ml and ejection fraction as percentage.

	Automatic vs Reference standard	Automatic vs Observer	Observer vs Reference standard
EDV			
R (CI for β)	0.98 (0.97,99)	0.98 (0.97,0.99)	0.99 (0.98,0.99)
SSE	15	14	11
B-A (95% CI)	1 (−32,31)	3 (−25,31)	4 (−22,30)
RPC	31	28	26
Abs diff	12 ± 10	11 ± 9	9 ± 11
ESV			
R (CI for β)	0.98 (0.96,0.99)	0.97 (0.94,0.98)	0.98 (0.97,0.99)
SSE	13	16	12
B-A (95% CI)	0 (−26,27)	5 (−29,40)	5 (−19,29)
RPC	26	34	24
Abs diff	10 ± 9	14 ± 12	10 ± 9
SV			
R (CI for β)	0.86 (0.73,0.93)	0.77 (0.57,0.87)	0.78 (0.60,0.89)
SSE	13	17	20
B-A (95% CI)	1 (−32,30)	2 (−39,35)	−1 (−39,38)
RPC	31	37	39
Abs diff	12 ± 11	15 ± 12	11 ± 17
EF			
R (CI for β)	0.90 (0.80,0.95)	0.87 (0.76,0.94)	0.90 (0.87,0.96)
SSE	5	6	5
B-A (95% CI)	−1 (−13,12)	−3 (−18,13)	−2 (−13,9)
RPC	13	16	11
Abs diff	5 ± 4	7 ± 4	8 ± 4

derived SAX and long-axis scans was 0.98, 0.99, 0.88 and 0.94 for EDV, ESV, SV and EF, respectively. The correlation between the manually segmented SAX scan and the automatic ones obtained using the proposed pipeline on the long-axis scan was 0.99, 0.98, 0.87 and 0.91 for EDV, ESV, SV and EF, respectively. The absolute volume differences between the manually segmented SAX scan and the automatic long-axis segmented scans was 12 ± 12 ml for EDV, 10 ± 8 ml for ESV, and 11 ± 11 ml for SV.

4. Discussion

We presented a fully-automatic pipeline that enables robust and accurate segmentation of the left ventricle endocardium and epicardium from long-axis cine MR scans. We demonstrated that the clinically relevant parameters can be accurately extracted from the two orthogonal horizontal and vertical long axis (HLA and VLA) scans without any manual interaction. A very good correlation with manual quantification was observed, with differences very close to those between the two observers.

The DSC overlap between the automatic and the reference standard manual segmentations showed very good agreement on both the end-diastolic (ED) and end-systolic (ES) phases, which averaged to 90%. The surface-to-surface distance between automatic and manual contours was around 2.75 mm, which is around 1.5 voxels. When the resolution of the scan is considered, this error is relatively small. It was also observed from Table 3 that the DSC values on the ES phase were slightly lower than on the ED phase. Even though the ES contours were improved by using the mitral valve detection step, the DSC values obtained are not as good as those on the ED phase. The lower DSC for the endocardial contours is mostly caused by the papillary muscles and trabeculae that appear more prominently on the ES phase. This results in some amount of intensity variation for the contour propagation step. Also, depending on the heart function, the ES phase has a lot of variations that, in general, causes lower DSC (can be seen on Fig. 9). However, the error on the automatically-obtained end-diastolic volumes (EDV) are very close to the interobserver variability.

With respect to the EF risk categorization, we have shown that our pipeline accurately classified 80% of the subjects to the correct category. With a κ agreement of 0.70, which is considered to have *substantial* agreement (Landis and Koch, 1977). This demonstrates that the proposed pipeline is quite robust. Note that the pipeline was tested on clinical data sets from multiple centers and the subjects included in this study have a broad range of cardiac anomalies.

The nine cases on which the pipeline performed sub-optimally were mainly caused by registration failure. A closer look at these cases showed that the registration failure was mainly because of poor image quality due to imaging artefacts. A number of commonly occurring cardiac MRI artefacts are described in the work of Ferreira et al. (2013).

Our pipeline is run independently on the two HLA and VLA scans, by doing so we are not affected by any misalignment due to patient movement, breath-hold position, or heart rate changes between the two acquisition. The proposed pipeline also has the potential to automatically detect LV segmentations that fail. As the pipeline is simultaneously run on the HLA and VLA scans, the corresponding endocardium and epicardium contour areas and major axis lengths are compared to each other. If one or more measures from the two views are significantly different, this indicates a clear failure of the pipeline. By setting a threshold on the difference between the measures on the HLA and VLA scans, it is also possible to indicate cases that may be considered to be of questionable quality.

The current work focuses on segmenting the LV as this is the structure that has been traditionally used to investigate the functional performance of the heart. The right ventricle (RV) is also an important structure for assessing a number of cardiac disorders, and MRI scans are being used routinely to investigate the RV (Haddad et al., 2008; Mertens and Friedberg, 2010). Automated segmentation of the RV has its challenges, the article from Petitjean et al. (2015) presents a number of methods that segment the RV from short-axis scans. Our proposed pipeline which uses the two orthogonal long-axis HLA and VLA scans and a geometric

assumption to estimate the LV volume can not be extended to the RV. The RV has a complex shape and using geometric models to estimate the RV volume is not reliable (Pujadas et al., 2004).

Another possible application of our automatic pipeline is for the purpose of feature tracking to assess wall motion abnormalities (Maret et al., 2009). It has been previously demonstrated that feature tracking can be performed on standard cine scans with comparable precision as on tagged sequences (Hor et al., 2010). Since our pipeline tracks the endocardium and epicardium contours over the entire cardiac cycle, it is possible to derive the strain parameters automatically. In this paper, however, we limited ourselves to the first step in such an analysis.

One of the limitations of our proposed pipelines is that it is only applicable for patients with normal heart topology. This approach can not be used on subjects that have a very different heart anatomy, for example, subjects with congenital heart defects.

In this paper we have demonstrated the feasibility of using cardiac long-axis HLA and VLA cine views for automatically deriving a number of clinical parameters. We also showed the accuracy of categorizing the subjects into different risk groups based on their ejection fraction. A limitation of our proposed method is that we derive volumetric measures from two orthogonal 2D views. However, Childs et al. (2011) and Huttin et al. (2015) have previously demonstrated that long-axis scans and the (manually) derived volumes can be used for fast and accurate measurements and have the advantage of relatively short scan acquisition time. We independently verified this comparison on a subset of 35 scans. The clinical parameters obtained using the short-axis scan and those derived from the HLA and VLA long-axis scans indicated that there was very close agreement between these two approaches (R between 0.99–0.87). This further supports the claim that clinical volumetric parameters derived from long-axis scans are as good as those obtained using SAX scans.

5. Conclusion

We are the first to develop and evaluate an automatic pipeline for left ventricle segmentation on horizontal and vertical long-axis cardiac cine MRI scans. We demonstrated that our pipeline was able to accurately quantify various clinical parameters using the two orthogonal long-axis scans. The pipeline proposed in this paper can therefore be used in large population-based studies.

Acknowledgments

We acknowledge the support from the Netherlands CardioVascular Research Initiative: the Dutch Heart Foundation (CVON 2012-06 Heart Brain Connection), Dutch Federation of University Medical Centres, the Netherlands Organisation for Health Research and Development, and the Royal Netherlands Academy of Sciences. The Heart Brain Connection collaborative research group further includes Mark A. van Buchem, Geert Jan Biessels, Hans-Peter Brunner la Rocca, Anton J. de Craen, Wiesje M. van der Flier, L. Jaap Kappelle, Simon P. Mooijaart, Wiro J. Niessen, Robert van Oostenbrugge, Albert de Roos, Albert C. van Rossum, and Mat J. Daemen.

The authors have no relevant conflicts of interest to disclose.

References

Alfakih, K., Reid, S., Jones, T., Sivananthan, M., 2004. Assessment of ventricular function and mass by cardiac magnetic resonance imaging. Eur. Radiol. 14 (10), 1813–1822.

Aljabar, P., Heckemann, R.A., Hammers, A., Hajnal, J.V., Rueckert, D., 2009. Multi-atlas based segmentation of brain images: atlas selection and its effect on accuracy. Neuroimage 46 (3), 726–738.

Bamberg, F., Kauczor, H.-U., Weckbach, S., Schlett, C.L., Forsting, M., Ladd, S.C., Greiser, K.H., Weber, M.-A., Schulz-Menger, J., Niendorf, T., et al., 2015. Whole–body MR imaging in the german national cohort: Rationale, design, and technical background. Radiology 277 (1), 206–220.

Bild, D.E., Bluemke, D.A., Burke, G.L., Detrano, R., Roux, A.V.D., Folsom, A.R., Greenland, P., Jacobs Jr, D.R., Kronmal, R., Liu, K., et al., 2002. Multi-ethnic study of atherosclerosis: objectives and design. Am. J. Epidemiol. 156 (9), 871–881.

Bloomer, T.N., Plein, S., Radjenovic, A., Higgins, D.M., Jones, T.R., Ridgway, J.P., Sivananthan, M.U., 2001. Cine MRI using steady state free precession in the radial long axis orientation is a fast accurate method for obtaining volumetric data of the left ventricle. J. Magn. Reson. Imaging 14 (6), 685–692.

Celermajer, D.S., Chow, C.K., Marijon, E., Anstey, N.M., Woo, K.S., 2012. Cardiovascular disease in the developing world: prevalences, patterns, and the potential of early disease detection. J. Am. Coll. Cardiol. 60 (14), 1207–1216.

Childs, H., Ma, L., Ma, M., Clarke, J., Cocker, M., Green, J., Strohm, O., Friedrich, M.G., 2011. Comparison of long and short axis quantification of left ventricular volume parameters by cardiovascular magnetic resonance, with ex-vivo validation. J. Cardiovasc. Magn. Reson. 13 (1), 40.

Dijkstra, E.W., 1959. A note on two problems in connexion with graphs. Numerische Mathematik 1 (1), 269–271.

Dulce, M.C., Mostbeck, G., Friese, K., Caputo, G., Higgins, C., 1993. Quantification of the left ventricular volumes and function with cine MR imaging: comparison of geometric models with three-dimensional data. Radiology 188 (2), 371–376.

Ferreira, P.F., Gatehouse, P.D., Mohiaddin, R.H., Firmin, D.N., 2013. Cardiovascular magnetic resonance artefacts. J. Cardiovasc. Magn. Reson. 15 (1), 41.

Fox, C.S., Gona, P., Hoffmann, U., Porter, S.A., Salton, C.J., Massaro, J.M., Levy, D., Larson, M.G., D'Agostino, R.B., O'Donnell, C.J., et al., 2009. Pericardial fat, intrathoracic fat, and measures of left ventricular structure and function the Framingham heart study. Circulation 119 (12), 1586–1591.

Haddad, F., Hunt, S.A., Rosenthal, D.N., Murphy, D.J., 2008. Right ventricular function in cardiovascular disease, part I. Circulation 117 (11), 1436–1448.

Hegenscheid, K., Kühn, J., Völzke, H., Biffar, R., Hosten, N., Puls, R., 2009. Whole-body magnetic resonance imaging of healthy volunteers: pilot study results from the population-based SHIP study. RoFo: Fortschritte auf dem Gebiete der Rontgenstrahlen und der Nuklearmedizin 181 (8), 748–759.

Hood, M.N., Ho, V.B., Smirniotopoulos, J.G., Szumowski, J., 1999. Chemical shift: the artifact and clinical tool revisited. Radiographics 19 (2), 357–371.

Hor, K.N., Gottliebson, W.M., Carson, C., Wash, E., Cnota, J., Fleck, R., Wansapura, J., Klimeczek, P., Al-Khalidi, H.R., Chung, E.S., et al., 2010. Comparison of magnetic resonance feature tracking for strain calculation with harmonic phase imaging analysis. JACC 3 (2), 144–151.

Huttin, O., Petit, M.-A., Bozec, E., Eschalier, R., Juillière, Y., Moulin, F., Lemoine, S., Selton-Suty, C., Sadoul, N., Mandry, D., et al., 2015. Assessment of left ventricular ejection fraction calculation on long-axis views from cardiac magnetic resonance imaging in patients with acute myocardial infarction. Medicine 94 (43), e1856.

Jefferson, A.L., Himali, J.J., Au, R., Seshadri, S., DeCarli, C., O'Donnell, C.J., Wolf, P.A., Manning, W.J., Beiser, A.S., Benjamin, E.J., 2011. Relation of left ventricular ejection fraction to cognitive aging (from the Framingham heart study). Am. J. Cardiol. 108 (9), 1346–1351.

Klein, S., van der Heide, U.A., Lips, I.M., van Vulpen, M., Staring, M., Pluim, J.P., 2008. Automatic segmentation of the prostate in 3D MR images by atlas matching using localized mutual information. Med. Phys. 35 (4), 1407–1417.

Klein, S., Pluim, J.P., Staring, M., Viergever, M.A., 2009. Adaptive stochastic gradient descent optimisation for image registration. Int. J. Comput. Vision 81 (3), 227–239.

Klein, S., Staring, M., Murphy, K., Viergever, M.A., Pluim, J.P., 2010. Elastix: a toolbox for intensity-based medical image registration. IEEE Trans. Med. Imaging 29 (1), 196–205.

Koikkalainen, J., Pollari, M., Lötjönen, J., Kivistö, S., Lauerma, K., 2004. Segmentation of cardiac structures simultaneously from short-and long-axis mr images. In: International Conference on Medical Image Computing and Computer-Assisted Intervention. Springer, pp. 427–434.

Lam, L., Suen, C.Y., 1997. Application of majority voting to pattern recognition: an analysis of its behavior and performance. IEEE Trans. Syst. Man Cybern. Part A 27 (5), 553–568.

Landis, J.R., Koch, G.G., 1977. The measurement of observer agreement for categorical data. Biometrics 159–174.

Li, C., Xu, C., Anderson, A.W., Gore, J.C., 2009. MRI tissue classification and bias field estimation based on coherent local intensity clustering: a unified energy minimization framework. In: Information Processing in Medical Imaging. Springer, pp. 288–299.

Maret, E., Todt, T., Brudin, L., Nylander, E., Swahn, E., Ohlsson, J.L., Engvall, J.E., 2009. Functional measurements based on feature tracking of cine magnetic resonance images identify left ventricular segments with myocardial scar. Cardiovasc. Ultrasound 7 (1), 1.

McClelland, J.R., Hawkes, D.J., Schaeffter, T., King, A.P., 2013. Respiratory motion models: a review. Med. Image Anal. 17 (1), 19–42.

Mendis, S., Puska, P., Norrving, B., 2011. Global Atlas on Cardiovascular Disease Prevention and Control. World Health Organization.

Mertens, L.L., Friedberg, M.K., 2010. Imaging the right ventriclecurrent state of the art. Nat. Rev. Cardiol. 7 (10), 551–563.

Metz, C., Klein, S., Schaap, M., van Walsum, T., Niessen, W.J., 2011. Nonrigid registration of dynamic medical imaging data using nD+t B-splines and a groupwise optimization approach. Med. Image Anal. 15 (2), 238–249.

Otsu, N., 1975. A threshold selection method from gray-level histograms. Automatica 11 (285–296), 23–27.

Petersen, S.E., Matthews, P.M., Francis, J.M., Robson, M.D., Zemrak, F., Boubertakh, R., Young, A.A., Hudson, S., Weale, P., Garratt, S., et al., 2016. UK biobank's cardiovascular magnetic resonance protocol. J. Cardiovasc. Magn. Reson. 18 (1), 1–7.

Petitjean, C., Dacher, J.-N., 2011. A review of segmentation methods in short axis cardiac MR images. Med. Image Anal. 15 (2), 169–184.
Petitjean, C., Zuluaga, M.A., Bai, W., Dacher, J.-N., Grosgeorge, D., Caudron, J., Ruan, S., Ayed, I.B., Cardoso, M.J., Chen, H.-C., et al., 2015. Right ventricle segmentation from cardiac MRI: a collation study. Med. Image Anal. 19 (1), 187–202.
Pruessmann, K.P., Weiger, M., Scheidegger, M.B., Boesiger, P., et al., 1999. SENSE: sensitivity encoding for fast MRI. Magn. Reson. Med. 42 (5), 952–962.
Pujadas, S., Reddy, G.P., Weber, O., Lee, J.J., Higgins, C.B., 2004. MR imaging assessment of cardiac function. J. Magn. Reson. Imaging 19 (6), 789–799.
Rohlfing, T., Brandt, R., Menzel, R., Russakoff, D.B., Maurer Jr, C.R., 2005. Quo vadis, atlas-based segmentation? In: Handbook of Biomedical Image Analysis. Springer, pp. 435–486.
Rohlfing, T., Russakoff, D.B., Maurer Jr, C.R., 2004. Performance-based classifier combination in atlas-based image segmentation using expectation-maximization parameter estimation. IEEE Trans. Med. Imaging 23 (8), 983–994.
Sakuma, H., Fujita, N., Foo, T., Caputo, G.R., Nelson, S., Hartiala, J., Shimakawa, A., Higgins, C., 1993. Evaluation of left ventricular volume and mass with breath-hold cine MR imaging. Radiology 188 (2), 377–380.
Sotiras, A., Davatzikos, C., Paragios, N., 2013. Deformable medical image registration: A survey. IEEE Trans. Med. Imaging 32 (7), 1153–1190.
Suri, J., Wilson, D., Laxminarayan, S., 2007. Handbook of Biomedical Image Analysis: Volume 3: Registration Models. Springer Science & Business Media, Berlin, Heidelberg.
Taylor Jr, H.A., Wilson, J.G., Jones, D.W., Sarpong, D.F., Srinivasan, A., Garrison, R.J., Nelson, C., Wyatt, S.B., 2005. Toward resolution of cardiovascular health disparities in African Americans: design and methods of the Jackson heart study. Ethnicity and Dis. 15 (4 Suppl 6), S6–4.
van Buchem, M.A., Biessels, G.J., Brunner la Rocca, H.P., de Craen, A.J., van der Flier, W.M., Ikram, M.A., Kappelle, L.J., Koudstaal, P.J., Mooijaart, S.P., Niessen, W., et al., 2014. The heart-brain connection: a multidisciplinary approach targeting a missing link in the pathophysiology of vascular cognitive impairment. J. Alzheimer's Dis. 42 (s4).
Victor, R.G., Haley, R.W., Willett, D.L., Peshock, R.M., Vaeth, P.C., Leonard, D., Basit, M., Cooper, R.S., Iannacchione, V.G., Visscher, W.A., et al., 2004. The Dallas heart study: a population-based probability sample for the multidisciplinary study of ethnic differences in cardiovascular health. Am. J. Cardiol. 93 (12), 1473–1480.
Warfield, S.K., Zou, K.H., Wells, W.M., 2002. Validation of image segmentation and expert quality with an expectation-maximization algorithm. In: Medical Image Computing and Computer-Assisted Intervention. Springer, pp. 298–306.